Claude Bédard[1], **Serafim Rodrigues**[1], **Noah Roy**[2], **Diego Contreras**[2] **and Alain Destexhe**[1]

Evidence for frequency-dependent extracellular impedance from the transfer function between extracellular and intracellular potentials

October 24, 2018

Abstract We examine the properties of the transfer function $F_T = V_m/V_{LFP}$ between the intracellular membrane potential (V_m) and the local field potential (V_{LFP}) in cerebral cortex. We first show theoretically that, in the subthreshold regime, the frequency dependence of the extracellular medium and that of the membrane potential have a clear incidence on F_T. The calculation of F_T from experiments and the matching with theoretical expressions is possible for desynchronized states where individual current sources can be considered as independent. Using a mean-field approximation, we obtain a method to estimate the impedance of the extracellular medium without injecting currents. We examine the transfer function for bipolar (differential) LFPs and compare to simultaneous recordings of V_m and V_{LFP} during desynchronized states in rat barrel cortex *in vivo*. The experimentally derived F_T matches the one derived theoretically, only if one assumes that the impedance of the extracellular medium is frequency-dependent, and varies as $1/\sqrt{\omega}$ (Warburg impedance) for frequencies between 3 and 500 Hz. This constitutes indirect evidence that the extracellular medium is non-resistive, which has many possible consequences for modeling LFPs.

Keywords: *Computational models; Local Field Potentials; EEG; Extracellular resistivity; Intracellular Recordings; Maxwell Equations*

1: Integrative and Computational Neuroscience Unit (UNIC), UPR2191, CNRS, Gif-sur-Yvette, France
E-mail: Destexhe@unic.cnrs-gif.fr
2: Department of Neuroscience, University of Pennsylvania, Philadelphia, USA.

1 Introduction

There is a widespread consensus that mechanisms for generating the intracellular electrical activity are very well understood, however not complete. In contrast, much less is known about the the genesis of extracellular potentials, which is a subject of intense research. This is associated to the difficulty in assigning measurements of the extracellular potentials to a unique neurophysiological generator, which makes modeling of LFP/EEG a complex issue. Some of these mechanisms are believed to be related to synaptic activity, synchronous population spikes, ephaptic interactions, ionic dynamics, morphological structure of the neurons and many other processes (reviewed in [Jefferys (1995), Nunez and Srinivasan (2006)]).

One of the characteristics of extracellular potentials is the very steep attenuation of "fast" events such as spikes, which are visible only within the immediate vicinity (a few microns) of the electrode. In contrast, "slow" events such as synaptic potentials are visible for much larger distances, typically a few hundred microns [Destexhe et al. (1999), Katzner et al. (2009)]. One way to explain this differential filtering is that the extracellular medium acts as a powerful low-pass filter [Bédard et al. (2004)]. However, this aspect is controversial because some measurements of brain conductivity did not display significant filtering effects [Logothetis et al. (2007)] while other measurements did [Ranck (1963), Gabriel et al. (1996)]. Some of these experiments [Gabriel et al. (1996)] used careful controls, such as correcting for electrode polarization, showing the different frequency-dependence of various biological tissues, but most importantly, the independent measurements of conductivity and permittivity with theoretical constraints (Kramers-Kronig relations) [Gabriel et al. (1996)]. The recent measurements

employed a sophisticated four-electrode measurement setup to yield more accurate measures [Logothetis et al. (2007)]. However, despite such controls, these measurements used current intensities that are much larger than biological sources, which may explain the discrepancy [Bédard and Destexhe (2009)].

In the present paper, we provide theoretical work and analyze experimental measurements to examine whether the extracellular medium is non-resistive. We examine a quantity which depends on the extracellular impedance, the transfer function between simultaneously recorded intracellular and extracellular potentials. We show theoretically that, in the linear regime and for desynchronized states, the transfer function calculated from an (intracellular) single recording site strongly depends on the extracellular impedance, and can therefore be used to investigate its frequency dependence. We show preliminary results from desynchronized states *in vivo*, which indicate that the extracellular medium is indeed frequency dependent. We relate these findings to previous work and discuss their possible implications for modeling LFPs/EEG.

2 Methods

The experimental data used in this paper were taken from a large database of cells [Wilent and Contreras (2005a), Wilent and Contreras (2005b)], in which we selected intracellular recordings with long periods of subthreshold activity, simultaneous with LFP recordings in the vicinity (1 mm) of the intracellular electrode, and in light anesthesia with desynchronized EEG.

2.1 Surgery and Preparation

Experiments were conducted in accordance with the ethical guidelines of the National Institutes of Health and with the approval of the Institutional Animal Care and Use Committee of the University of Pennsylvania. Adult male Sprague-Dawley rats (300-350g, n=35) were anesthetized with isoflurane (5% for induction, 2% during surgery), paralyzed with gallamine triethiodide, and artificially ventilated. End tidal CO_2 (3.5-3.7%) and heart rate were continuously monitored. Body temperature was maintained at $37^\circ C$ via servo-controlled heating blanket and rectal thermometer (Harvard Apparatus, Holliston, MA). The rat was placed in a stereotaxic apparatus and a craniotomy was made directly above the barrel cortex (1.0-3.0 mm A/P, 4.0-7.0 mm M/L), and the dura was resected. The cisterna magna was drained to improve stability. For intracellular recordings, additional measures were taken to improve stability, including dexamethasone (10 mg/kg, i.p.) to reduce brain swelling, hip suspension, and filling the craniotomy with a solution of 4% agar.

2.2 Electrophysiological Recordings

Recordings of local field potentials (LFPs) across the cortical depth were performed with 16-channel silicon probes (Neuronexus, Ann Arbor, MI). Probe recording sites were separated by 100 μm and had impedances of 1.5-2.0 MΩ at 1 kHz. The probe was lowered into the brain under visual guidance, oriented normal to the cortical surface, until the most superficial recording site was aligned with the surface. All neurons were regular-spiking cells, and had spikes with about 2 ms width, so they were presumably excitatory. All LFP signals shown here were obtained by pairs of closely-located (400-500 μm apart) electrodes arranged vertically (surface-depth), and were amplified and band-pass filtered at 0.1 Hz–10 kHz (FHC, Inc., Bowdoinham, ME).

Intracellular recordings were performed in barrel cortex with glass micropipettes pulled on a P-97 Brown Flaming puller (Sutter Instrument Company, Novato, CA). Pipettes were filled with 3M potassium acetate and had DC resistances of 60-80 MΩ. A high-impedance amplifier (low-pass filter of 5 kHz) with active bridge circuitry (Neurodata, Cygnus Technology, Inc., Delaware Water Gap, PA) was used to record and inject current into cells. Vertical depth was measured by the scale on the micromanipulator. A Power 1401 data acquisition interface and Spike2 software (Cambridge Electronic Design, Cambridge, U.K.) were used for data acquisition.

2.3 Analysis and simulations

All simulations and analyses were realized using MATLAB (Mathworks Inc, Natick, MA), except for compartmental model simulations (see below).

The analysis of the PSD was performed using two different methods. A constrained nonlinear least square fit of the analytic expressions for different possible transfer functions (see Eq. 27 and Eq. 22 in Results) was performed to the transfer function calculated from experimental data. The fit was constrained to frequencies between 3 Hz and 500 Hz and the parameters of the

transfer functions were constrained to the physiological range (see Results for details).

Because the PSD and calculated transfer functions had large variance, two different methods were used to perform the fitting. First, a polynomial averaging algorithm was used to calculate the mean value of the PSD, and the fit was performed against this mean value (see details in Appendix B). Second, a moving average window procedure which consisted of partitioning the data set into five epochs (corresponding to about 7.7 sec for one cell and about 4.4 sec for the second cell, and additionally applied a Hanning window to each epoch (a Hamming window was tested as well, and gave similar results). This method markedly reduces the variance of the PSD and of the transfer function. Other choices for window length were also tested and yielded similar results as those shown in the figures (not shown).

2.4 Compartmental model simulations

Compartmental models were simulated using the freely-available NEURON simulation environment [Hines and Carnevale (1997)]. A 16-compartment "ball-and-stick" model was simulated, based on a soma (area of 500 μm^2) and 15 dendritic compartments of equal length (46.6 μm) and tapering diameter (from 4 μm at the soma up to 1 μm at the distal tip), so that the total cell area was of 6000 μm^2. Each compartment had passive properties, with axial resistivity of 250 Ω·cm, specific capacitance of 1 μF/cm^2, resting membrane conductance of 0.45 mS/cm^2 and reversal potential of -80 mV.

To simulate high-conductance states similar to *in vivo* measurements, each dendritic compartment contained two randomly fluctuating synaptic conductances (model from [Destexhe et al. (2001)] which were adjusted so that the mean excitatory and inhibitory conductances were respectively of 0.73 and 3.67 times the resting conductance. These values represent mean values of the "spontaneous" synaptic activity during activated states *in vivo*, according to intracellular measurements (see details in [Destexhe et al. (2003)]). We verified that using these parameters, the subthreshold V_m activity of the cell was conform to typical intracellular measurements during desynchronized-EEG states, as for example in the experiments reported here.

In a separate set of simulations, the synaptic inputs were present only in the most distal compartment. In this case,

all synaptic conductances were set to zero in all other compartments.

The LFP generated by this compartmental model was calculated at the level of the stem dendrite, 50 μm lateral to the dendritic axis, assuming a purely resistive medium, according to the expression:

$$V_{LFP} = \frac{R_e}{4\pi} \sum_j \frac{I_j}{r_j}, \tag{1}$$

where $R_e = 230$ Ω·cm is the extracellular resistivity [Ranck (1963)], I_j is the total membrane current of compartment j, and r_j is the distance between compartment j and the extracellular position where the LFP is evaluated. The LFP of the full model was compared to the LFPs calculated from each individual current source similar to above, with $V_{LFP}^{(j)} = \frac{R_e}{4\pi} \frac{I_j}{r_j}$.

3 Theory

In this section we formulate a theoretical relationship between extracellular and intracellular sub-threshold voltage activity. We consider a linear electromagnetic regime, which is defined by the fact that the linking equations are linear in frequency space. In such case we have $\mathbf{j}_f = \sigma_f \mathbf{E}_f$, $\mathbf{D}_f = \varepsilon_f \mathbf{E}_f$ and $\mathbf{B}_f = \mu_f \mathbf{H}_f$ where the second-order symmetric tensors σ_f, ε_f and μ_f do not depend on $\mathbf{E}_f$ and $\mathbf{H}_f$. σ_f, ε_f and μ_f depend on position in general. In other words, we will work in the subthreshold voltage range, for which we assume linear current-voltage relations, and that conductances are not voltage dependent. Henceforth, we will refer to this dynamical state as "linear regime". We also assume that the cortical tissue is macroscopically isotropic, in which case the tensors become scalar functions.

We will also formulate the model in the frequency domain, to easily enable comparison between the amount of intracellular and extracellular signal within each frequency band, which is readily accessible from experimental data. The advantage of this approach is simplicity as it avoids tackling directly the different time scales inherently associated to LFP/EEG signals, many of which are not yet understood. For example, it is known that LFP/EEG signals are composed of mixed-mode oscillations, however the origins and transitions between these modes are not yet explained [Erchova and McGonigle (2008)]. The choice of working in the frequency domain also seems natural because the differential equations describing electric potentials transform into algebraic equations in frequency space.

The formulation of the relation between transmembrane (V_m) and extracellular (V_{LFP}) activity requires to derive the transfer function, F_T, that measures the ratio between the impedance of the cellular membrane and extracellular medium. To obtain this, we start from a general formalism where V_{LFP} is expressed as a function of a large number of current sources located at different positions in extracellular space (Section 3). We then show under what conditions this formalism can reduce to a single current source, and derive the impedance for this current source (Section 3.3) and derive the corresponding transfer functions (Sections 3.4 to 3.5).

In the following, we use the notation $F(f)$ or F_f to denote the function F in Fourier space with frequency f and $\omega = 2\pi f$.

3.1 General model with multiple current sources

We start from the general model in Fourier space:

$$V_{LFP}(r_i, f) = \sum_{j=1}^{N} \frac{R_j}{d_{ij}} Z_j^{med}(f) I_j(f) , \qquad (2)$$

where $V_{LFP}(r_i, f)$ is the extracellular potential at a position r_i as resulting from a set of N monopolar current sources $I_j(f)$. R_j is a constant, d_{ij} is the distance between source j and position r_i, and Z_j^{med} is the impedance of the extracellular medium around source j. This model is based on the property that any charge distribution in space and frequency can be expressed as a sum of monopolar sources. This therefore applies to complex current distributions in the complex dendritic structures of many neurons surrounding the recording site r_i (see Fig. 1A), and thus, this formalism is general.

If we assume that the extracellular medium is electrically homogeneous, the extracellular impedance Z_j^{med} is the same for every pair of points i, j, and the local field potential becomes:
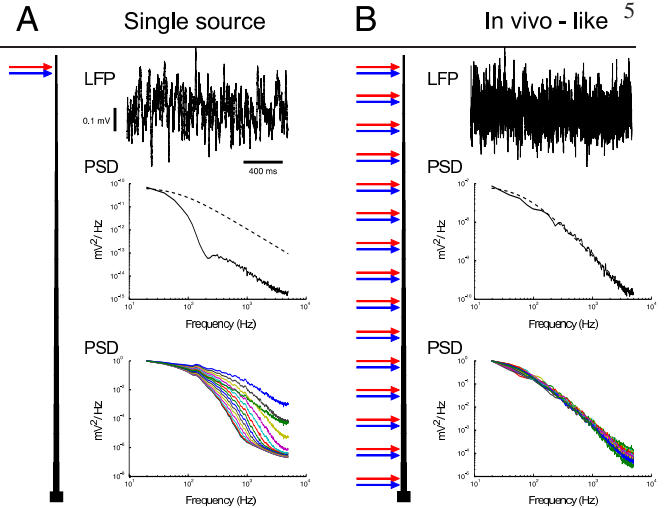
$$V_{LFP}(r_i, f) = Z^{med}(f) \sum_{j=1}^{N} \frac{R_j}{d_{ij}} I_j(f) \qquad (3)$$

We also assume that the network activity is of low correlation, as typically found during desynchronized network states *in vivo*, such as in awake animals, or during the "up-states" of anesthesia. In such states, it was shown that the activity is very irregular with low levels of correlation between cortical neurons [Destexhe et al. (1999), Gawne and Richmond (1993), Steriade et al. (2001b), Zohary et al. (1994)]. As a
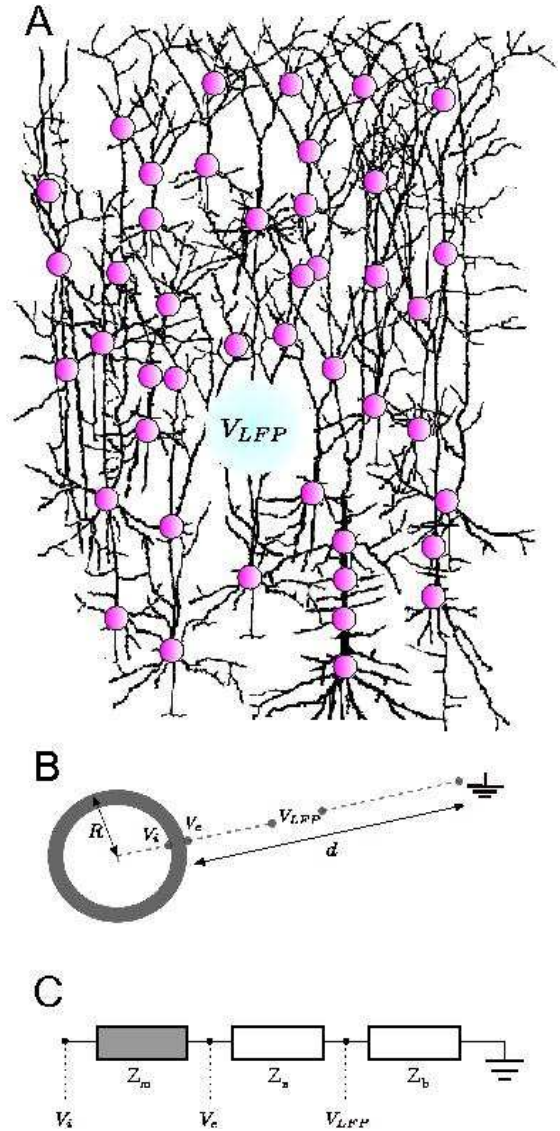
Fig. 1 Arrangement of potentials and impedances. A. Scheme of the general model where the local field potential (V_{LFP}) is generated by a large number of individual monopolar current sources (red) distributed in soma and dendrites of neurons in the network. If the activity of these current sources is desynchronized, the system can reduce to a single current source using a mean-field approximation. B. Scheme of an individual current source, which is assumed to be of spherical symmetry with homogeneous extracellular medium, so that there is no position-dependence of conductivity or permittivity. V^i and V^e are the electric potentials, respectively inside and outside of the membrane, relative to a reference potential $R_f^\infty = 0$ situated at an infinite distance. The membrane potential V_m is the difference between V_i and V_e. V_{LFP} is the local field potential, which is the voltage difference between a point P in extracellular space and R_f^∞. C. Equivalent electrical circuit for each current source, where Z_m is the impedance of the membrane, while Z_a and Z_b are impedances of the extracellular medium.

consequence, we can consider that the dendritic structure is bombarded by noisy synaptic events that are essentially uncorrelated, and if we assume that this activity primes over the deterministic link between individual current sources (see Section 3.2 for a test of this assumption),

then the field produced by the ensemble of N current sources is equivalent to the field produced by independent sources. the variables $\frac{R_j}{d_{ij}}$ and I_j can be considered as statistically independent, and by averaging over the ensemble of current sources, we obtain:

$$V_{LFP}(r_i, f) = Z^{med}(f) \sum_{j=1}^{N} \frac{R_j}{d_{ij}} I_j(f) = Z^{med}(f)\, \bar{R}_D\, \bar{I}(f) .$$

$$(4)$$

Here, the LFP has been expressed as a function of a "mean current source" (in the spatial sense) $\bar{I}(f) = N <I_j(f)>|_j$ and where $\bar{R}_D = <\frac{R_j}{d_{ij}}>|_j$ [1]. This formulation is equivalent to a mean-field theory expressed in Fourier space and where we consider the LFP as generated by the mean current source contribution.

3.2 Testing the assumptions of the formalism

To verify some of the assumptions of the formalism, we have simulated a ball-and-stick dendritic model subject to fluctuating synaptic conductances (Fig. 2). In a first set of simulations, the synaptic conductances (model from [Destexhe et al. (2001)]) were located only at a single dendritic location. This case produced LFPs which were markedly filtered by the dendritic structure (Fig. 2A, middle panel), as described previously [Pettersen and Einevoll (2008)]. This type of filtering is due to the fact that in dendritic structures, the return current (which participates to generate the LFP) is filtered by the membrane. In another set of simulations, we have considered a more realistic situation in which the synaptic conductances were located at all locations of the dendritic structure, so that the total conductance matches that measured experimentally *in vivo* [Destexhe et al. (2003)]. In this case, the filtering due to morphology was negligible (Fig. 2B, middle panel), presumably because synaptic currents largely dominate over axial currents. These simulations suggest that the filtering due to morphology can be neglected for *in vivo*–like conditions, and that in such conditions, the filtering must come from another origin, such as the extracellular medium.

To test the validity of a mean-field approximation, we have plotted the PSD of the LFP generated by each individual source in the ball-and-stick neuron (Fig. 2A,B, bottom panels). In the case the synaptic current is located at a single dendritic location, the PSDs of individual sources are all different (Fig. 2A, bottom), because of the filtering due to the morphology. However, in the case of

Fig. 2 Test of the assumptions of the formalism using a ball-and-stick model. A. Top: scheme of the model. Excitatory (blue) and inhibitory (red) random synaptic conductances (model taken from [Destexhe et al. (2001)]) were inserted in the distal compartment of a ball-and-stick model with 16 compartments (see Methods). Middle: LFP calculated from the total membrane currents, at 50 μm from the neuron. Middle: PSD of the LFP, which showed a marked filtering due to the neuronal morphology, as described previously [Pettersen and Einevoll (2008)]. Bottom: PSDs obtained from the LFP of each individual source. B. Same simulation as in A, but the random synaptic inputs were distributed in all dendritic compartments and were matched to the the conductance state observed *in vivo*. Middle: the filtering due to morphology was negligible in this case. Bottom: individual PSDs are very similar, suggesting that a mean-field approximation is justified in this case. The dotted curves represent the optimal fit to the PSD in B, using a Lorentzian function $1/(1+\omega^n\tau^n)$ with $n = 1.8$ and rescaled to the maximum of each PSD.

distributed current sources, the PSDs of different current sources are very similar (Fig. 2B, bottom). This similarity also extended to LFPs calculated from different locations in extracellular space, which produced LFPs of different amplitudes, but with almost superimposable PSDs (not shown). These simulations suggest that, for in *in vivo*–like states, a mean-field approximation is reasonable.

3.3 Membrane impedance for a spherical source in the linear regime

In the previous sections, we assumed that the LFP generated in desynchronized network states has equivalent properties to that produced by a "mean current source". We now calculate the membrane impedance for an individual current source of spherical symmetry, embedded in a medium which is homogeneous/isotropic and continuous, and with electric parameters σ_f, ε_f [2]. The

---

[1] Note that for desynchronized activity, we expect that such a spatial average will be of small amplitude, as indeed typically found for the "desynchronized EEG" condition investigated here.

[2] Note that we keep the electric parameters frequency dependent, to keep the expressions as general as possible. In addition, the theory can easily be generalized to multipoles, as any multipole

cell is represented by an RC circuit where the membrane potential is expressed as the difference $V_m = V_i - V_e \approx -70\ mV$ (Fig. 1B). At the resting membrane potential, there is a net negative charge Q_- inside, which is perfectly balanced with a net positive charge Q_+ on the external surface of the membrane, such that $Q_- + Q_+ = 0$. In this situation, the electric field **E** produced by the cell in the medium is null, which implies that $V_e = V_f^\infty = 0$, where V_f^∞ is the reference potential at infinite distance from the source.

Suppose that a small excess of positive charge is injected inside the cell. Due to this excess of charge, an electric field **E** will instantaneously appear in extracellular space. An electric current will also appear to restore the equilibrium (and therefore will give rise to a variation of the electric field). The current produced depends on the physical and biological characteristics of the membrane, which will determine the time evolution of the electric field. The current is given by:

$$I_r = \sum_{i=1}^{N} g_i\ (t, V_m)(V_m(t) - E_i)$$

$$I_c = C_m \frac{dV_m}{dt}$$

$$I_m = I_r + I_c$$

(5)

where I_r and I_c are the ionic and capacitive currents, respectively. The index i represents the different membrane conductances g_i, with their reversal potential E_i, and C_m is the membrane capacitance.

In the following, we will assume that the excess of charge remains small and varies around a stationary mean value, so that we can can neglect the time variations of conductances and of the V_m (ΔV_m), with $\partial g_j^i / \partial V_m \approx 0$. In this case, we can consider that the conductances are only function of the mean value of the V_m. This is equivalent to assume that, in the subthreshold regime, the conductances are not dependent on the potential, and that the reversal potentials E_i are constant. This is valid if the impact of ionic concentration changes on E_i are negligible compared to the voltage variations.

configuration can be decomposed in a sum of monopoles, and to multiple sources using the linear superposition principle.

Under these approximations, we can write:

$$\Delta I_r = \sum_{i=1}^{N} g_i\ (\langle V_m \rangle |_t)\Delta V_m$$

$$\Delta I_c = C_m \frac{d\Delta V_m}{dt}$$

(6)

$$\Delta I_m = \Delta I_r + \Delta I_c$$

(7)

Here, we have a linear system of equations with time-independent coefficients. By expressing the variation of current produced by the cell as a function of the variation of membrane voltage, in Fourier space, we obtain:

$$\Delta I_r(f) = G_m \Delta V_m(f)$$

$$\Delta I_c(f) = i\omega C_m \Delta V_m(f)$$

(8)

$$\Delta I_m(f) = \Delta I_r(f) + \Delta I_c(f)$$

where

$$G_m = \sum_{i=1}^{N} g_i\ .$$

The impedance of the membrane is given by:

$$Z_m(f) = \frac{\Delta V_m(f)}{\Delta I(f)} == \frac{R_m}{1 + i\omega \tau_m}$$

(9)

where $R_m = \frac{1}{G_m}$.

We next define the theoretical transfer function, which provides a relation (in this case, in the frequency domain) between LFP and V_m, as $F_T(\mathbf{r}, f) = \frac{V_m}{V_{lfp}}(\mathbf{r}, f)$. Having defined above the impedance of the membrane we now require to define the impedance of the medium to fully characterize the transfer function. Consequently, in subsequent sections, we define the transfer function in general form and we then consider particular cases due to different recordings montages (bipolar and monopolar) and various types of media.

3.4 Computing the transfer function of each current source.

In this section, we calculate separately the two transfer functions:

$$F_T^{(1)}(f) = \frac{V_m(f)}{V_e(f)}$$

and

$$F_T^{(2)}(d,f) = \frac{V_e(f)}{V_{LFP}(d,f)} \ .$$

$F_T^{(1)}(f)$[3] can be calculated from the equivalent circuit shown in Fig. 1C. We have the following relations:

$$Z_{med}(R,f) = Z_a(d,f) + Z_b(d,f) \tag{10}$$

$$V_m(f) = V_i(f) - V_e(f) \tag{11}$$

$$\frac{V_i(f)}{Z_m(f) + Z_{med}(R,f)} = \frac{V_e(f)}{Z_{med}(R,f)} \tag{12}$$

where R is the radius of the current source and d is the distance relative to the center of the source. It follows that

$$F_T^{(1)}(f) = \frac{V_m(f)}{V_e(f)} = \frac{Z_m(f)}{Z_{med}(R,f)} \tag{13}$$

$F_T^{(2)}(d,f)$ can also be calculated based on the equivalent circuit of Fig. 1C:

$$F_T^{(2)}(d,f) = \frac{V_e(f)}{V_{LFP}(d,f)} = \frac{Z_a(f) + Z_b(d,f)}{Z_b(d,f)} \tag{14}$$

We note that if Z_a and Z_b have the same frequency dependence, for example f^n, then $F_T^{(2)}$ is independent of frequency when the medium is macroscopically homogeneous. For example, if both media have a Warburg impedance ($Z \sim 1/\sqrt{f}$) or capacitive impedance ($Z \sim 1/f$), the function $F_T^{(2)}$ has the same value as for the case of a resistive medium (frequency independent impedance). For a spherical source and for an extracellular position at a distance d from the center of the source, we have:

$$F_T^{(2)}(\mathbf{r},f) = \frac{V_e(f)}{V_{LFP}(\mathbf{r},f)} = \frac{d}{R} \tag{15}$$

where R is the radius of the current source. In this relation, the resistance of a spherical shell of radius r in an isotropic and homogeneous medium of infinite dimension equals $\frac{1}{4\pi\sigma r}$, which corresponds to the sum $Z_a + Z_b$ when $r = R$ and Z_b when $r = d$.

In the case of a heterogeneous isotropic medium, we have [Bédard and Destexhe (2009)]:

$$Z(r,f) = \frac{1}{4\pi\sigma_z(R)} \int_r^\infty dr' \frac{1}{r'^2} \frac{\sigma_f(R) + i\omega\,\varepsilon_f(R)}{\sigma_f(r') + i\omega\,\varepsilon_f(r')} \tag{16}$$

for a spherical and isopotential source. σ_z represents the complex conductivity. In the absence of spherical symmetry and with non-isopotential sources, it is necessary, in general, to solve differential or integral equations derived from Maxwell equations in the quasi-static regime (neglecting electromagnetic induction; see [Chari and Salon (1999)]).

It is important to note that the expressions above for the transfer function are independent of the particular frequency spectrum of the current sources.

3.5 Frequency dependence of differential (bipolar) recordings

If the power spectral density (PSD) of the LFP signal varies as $1/f^\gamma$ where $\gamma \geq 1$ (for monopolar LFP recordings), then the energy associated to the signal would necessarily be infinite, which is of course physically impossible. In fact, according to a model developed previously (see Eqs. 53–54 in [Bédard and Destexhe (2009)]), a more accurate relationship between the extracellular medium's properties and the mean V_f is given by the following expression

$$V(\mathbf{r},f) = \frac{\kappa_i(\mathbf{r})}{f^{\gamma/2} + a_i} \ . \tag{17}$$

where a_i is negligible for frequencies larger than 1 Hz and smaller than about 500 Hz (because LFPs are usually considered up to 500 Hz). Note that the PSD is proportional to the square of $V(f)$ and will thus scale as $1/f^\gamma$ in this case. The PSD is also independent of the position (homogeneous medium).

The values of constants κ_i and a_i represent respectively the proportionality constant for each electrode i, which depends on the intensity of the field for large frequencies, and the natural limit of the value of the voltage for very low frequencies (which limits the energy of the system). In general, these constants depend on electrode position, and therefore when one takes the difference between two electrodes, we have:

$$V_{diff}(f) = V_{LFP}^{(1)}(f) - V_{LFP}^{(2)}(f) = \frac{\kappa_1}{f^{\gamma/2} + a_1} - \frac{\kappa_2}{f^{\gamma/2} + a_2}.$$

---

[3] Note that the notation $F_T^{(n)}$ stands for different functions and not for n^{th} order derivative.

(18)

If the signal intensities of the two electrodes are comparable for large frequencies, we have necessarily $\kappa_1 \approx \kappa_2$, such that the differential or bipolar signal (difference between two nearby extracellular electrodes (very correlated signals), will have the following form, on average:

$$V_{diff}(f) \approx \kappa_1 \cdot \frac{a_2 - a_1}{(f^{\gamma/2} + a_2)(f^{\gamma/2} + a_1)} \approx \frac{\hat{\kappa}}{f^{\gamma}}. \qquad (19)$$

where $\hat{\kappa} = \kappa_1(a_2 - a_1)$ and for $f > 1\,Hz$ and $f < 500\,Hz$. Thus, if monopolar LFPs have a PSD which varies as $1/f^{\gamma}$, one can have a PSD in $1/f^{2\gamma}$ in bipolar recordings.

4 Numerical simulations of transfer functions

In this section, we present simple numerical simulations to illustrate how the transfer function is influenced by the frequency dependence of the cellular membrane, that of the medium, and of the recording configuration.

4.1 Resistive membrane with homogeneous/isotropic resistive medium

As a first and simplest case, suppose we have a resistive membrane (the membrane capacitance is neglected), embedded in a homogeneous resistive medium. In this case, the resistive medium is described by Laplace equation, and we have:

$$F_T(f) = F_T^{(1)}(f) \cdot F_T^{(2)}(f) = \frac{R_m}{R_{med}} \cdot \frac{R}{d}, \qquad (20)$$

where R is the radius of the source, R_m is the membrane resistance, R_{med} is the resistance of the medium, and d is the distance from the LFP measurement site to the center of the source.

This case, however, is not very realistic because the membrane capacitance is neglected. In the following sections, we consider more elaborate membranes and different extracellular media.

4.2 Capacitive effects of membranes in homogeneous/isotropic resistive media

We now consider a membrane with capacitive effects described by a simple RC circuit, together with a resistive medium. In this case, we have:

$$F_T(f) = F_T^{(1)}(f) \cdot F_T^{(2)}(f) = \frac{Z_m(f)}{R_{med}} \cdot \frac{R}{d}, \qquad (21)$$

where the parameters are as described above, with $Z_m(f)$ the membrane impedance. Thus, according to Eq. 9, we have the following transfer function:

$$F_T^s(f) = \frac{R_m}{R_{med}} \cdot \frac{1}{1 + i\omega\tau_m} \cdot \frac{R}{d}. \qquad (22)$$

where τ_m is the membrane time constant. This transfer function is depicted in Fig. 3A.

The transfer function can also be calculated for a "non ideal" membrane, with a more realistic RC circuit model where the capacitance is non-ideal and does not charge instantaneously (see details in [Bédard and Destexhe (2008)]; see also Appendix A). Considering such a non-ideal membrane with a resistive medium, we have:

$$F_T^N(f) = \frac{R_m}{R_{med}} \cdot \frac{1}{1 + i\frac{\omega\tau_m}{1 + i\omega\tau_{MW}}} \cdot \frac{R}{d} \qquad (23)$$

where τ_{MW} is the Maxwell-Wagner time of a non-ideal capacitance. Note that when $\tau_{MW} = 0$, we recover the case above for an ideal membrane. This transfer function is represented in Fig. 3A. The transfer function is in general monotonic (and scales close to $1/f^2$).

Interestingly, there is a phase resonance for non-ideal membranes (see ($\star$) in Fig. 3B). The physical origin of this phase resonance in the non-ideal cable is that the membrane is quasi-resistive at low ($\simeq 0$) and high frequencies (100 Hz) (see Eq. 33), so that the absolute value of the phase must necessarily pass through a maximum[4]

4.3 RC membrane in homogeneous/isotropic non-resistive medium

We now focus on non-resistive media by providing a transfer function for which the functional form should be observable from extracellular measurements. We consider the simplest case scenario of only linear subthreshold regime where the membrane is described by a simple RC circuit embedded in a medium with impedance $Z(f)$. In this case, the transfer function for a mono-polar extracellular recording is given by:

$$F_T(f) = R_m \cdot \frac{1}{Z(f)\,(1 + i\omega\tau_m)} \cdot \frac{R}{d}, \qquad (24)$$

---

[4] Every positive continuous function defined on a compact domain has necessarily a maximum inside that domain.

If the impedance of the medium is $\frac{\kappa}{f^{\gamma/2}-a_i}$ and $\gamma \geq 1$, where κ is a complex constant, the monopolar and bipolar transfer functions are respectively:

$$F_T^{mono}(f) \approx \frac{R_m}{\kappa} \cdot \frac{(f)^{\gamma/2}}{1+i\omega\tau_m} \cdot \frac{R}{d}.$$
$$F_T^{diff}(f) \approx \frac{R_m}{\hat{\kappa}} \cdot \frac{f^{\gamma}}{1+i\omega\tau_m} \cdot \frac{R}{d}. \tag{25}$$

The differences between monopolar and bipolar transfer functions are explained in Section 3.5. In Fig. 3C, we show few examples of such a case with different values of the membrane time constant τ_m. We observe that the modulus of the transfer function can present a maximum which depends on τ_m, and therefore of the level of activity or the "conductance state" of the membrane.

5 Comparison with experimental results

In this section, we test the resistive or non-resistive nature of the extracellular medium by evaluating the transfer function from experimental data and compare with theoretical estimates. However, we note that in our experiments we use bipolar LFPs recorded in rat barrel cortex, simultaneously with intracellular recordings in the same cortical area. Since the LFP recordings are bipolar, we use the following form (see Section 4.3):

$$F_T^{(diff)}(f) = \frac{R_m f^{\gamma}}{\hat{\kappa}(1+i\omega\tau_m)} \cdot \frac{R}{d}, \tag{26}$$

with $Z(f) = \frac{\kappa}{f^{\gamma/2}-a_i}$ and $\gamma \geq 1$. Here, d is the distance between the recording site and the source (approximately 1 mm in these experiments).

In the particular case of a Warburg impedance ($\gamma = 1$), we have:

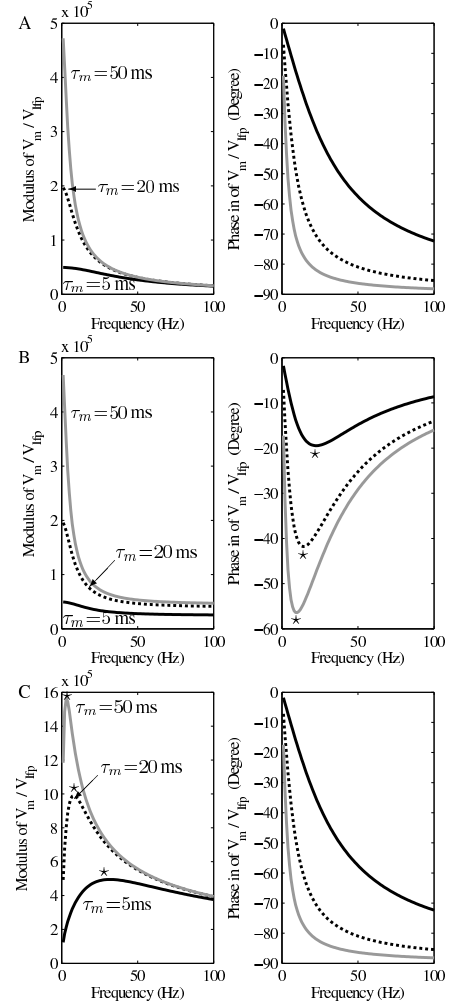$$F_T^{(diff)}(f) = \frac{R_m f}{\hat{\kappa}_w(1+i\omega\tau_m)} \cdot \frac{R}{d}, \tag{27}$$

where $\hat{\kappa}_w$ is a complex constant because a Warburg impedance is such that $Z(f) = \frac{a+ib}{\sqrt{f}}$. For a quasi-resistive medium $Z(f) = \frac{\kappa}{f^{\gamma}-a_i}$ with γ very close to zero, we have:

$$F_T^{(diff)}(f) = \frac{R_m}{\hat{\kappa}_r(1+i\omega\tau_m)} \cdot \frac{R}{d}, \tag{28}$$

where $\hat{\kappa}_r$ is a real constant.

Finally, in the case of a purely capacitive medium, $\gamma = 2$ and we have:

$$F_T^{(diff)}(f) = \frac{R_m f^2}{\hat{\kappa}_c(1+i\omega\tau_m)} \cdot \frac{R}{d}, \tag{29}$$

Fig. 3 Amplitude and phase of the transfer function F_T as a function of frequency for different models and for mono-polar electrode montage. In all cases the transfer function was estimated for a distance of 30 μm from a spherical source of 10 μm radius. A. Standard RC membrane model with $C_m = 10^{-2}$ F/m^2 and various configurations for membrane time constant τ_m. The extracellular medium conductivity is 0.3 S/m. B. Non-ideal membrane model (see [Bédard and Destexhe (2008)]) with same parameters as in A, and with a Maxwell-Wagner time $\tau_{MW} = 5$ ms (see Appendix A). The extracellular medium is also resistive in this case. Surprisingly, we observe a resonance in the phase of the transfer function as indicated by ($\star$). C. Standard RC membrane model together with a medium described by a Warburg Impedance $\frac{e^{i\phi}}{4\pi\sigma\sqrt{f}}$ where ϕ is frequency independent. We have taken $\phi = 0$ to illustrate the differences between this type of impedance compared to a resistive medium. ϕ will be different than zero in general, with no change to the modulus. Note that there is a peak in amplitude of the absolute value of the transfer function that increases and shifts to lower frequencies as τ_m increases; $\star$ indicates a resonance.

where $\hat{\kappa}_r$ is a purely imaginary constant in this case.

We now compare Eqs. 27–29 with the experimental measurements. We have analyzed four neurons in which simultaneous V_m and (bipolar) V_{LFP} were obtained from rat barrel cortex *in vivo*. Because the theoretical estimates

are for linear regime activity, our analysis must avoid any possible interference with spikes, and focus solely on long periods of subthreshold activity as marked by the grey shaded boxes superimposed on the V_m and LFP traces (see Fig. 4). The bottom panels of Fig. 4 show the PSD of the V_m and of V_{LFP}, which display similar frequency-scaling exponents. Note that the exponent values of V_m activity lie within the range identified for other anesthetic conditions, for which the V_m exponent varies between -2 and -3 [El Boustani et al (2009), Rudolph et al. (2005)]

To compute the transfer function from these data sets, we evaluate the ratio between the absolute value of the Fourier transform of both V_m and LFP as shown in Fig. 5A (light grey curves), which corresponds to the data of Fig. 4. As suggested by this similar scaling (bottom panel of Fig. 4), the transfer function of the data $F_T^{(diff)}$ has a mean value that is approximately constant (slope zero) for a large frequency range (about 10 Hz to 500 Hz) (Fig. 5A-B).

We performed a constrained nonlinear least square fit for the three transfer functions (Eqs. 27, 28 and 29) to the calculated data transfer function $F_T^{(diff)}$ for the frequency range between 3 Hz and 500 Hz. The membrane time constant was constrained to physiological range, $\tau_m \in [5\ ms, 50\ ms]$, whereas the lumped parameter, $\alpha = \frac{R_m R}{\hat{k} d}$, was allowed to vary for a large set, $\alpha \in [0, 10^3]$. Note that we chose not to fit all the parameters (R_m, R, $\hat{k}$ and d) as some of these parameters are related (e.g. R_m and τ_m) and there is an indeterminacy about these parameters because they are lumped. In addition, some parameters will vary from experiment to experiment. For instance, electrode coefficients, size of the measured cell, diffusion constants (embedded in the parameter $\hat{k}$, as indicated by Eqs. 53-54 in [Bédard and Destexhe (2009)]) will vary across different experiments. To fit all these parameters, a different experimental protocol would be required to gather the necessary data to disambiguate them. Hence, we decided to lump them into the single parameter α and also for the fitting purpose we consider α and τ_m to be independent.

To ensure soundness in the parameter fitting, we employed two different averaging techniques to the transfer function F_T^{diff} (see Methods). Polynomial averaging techniques (see Appendix B) are known to produce robust results when the variance of the signal is very high [Press et al. (2008)]. This method is applied here in the frequency domain, and virtually suppresses all of the variance of the transfer function (Fig. 5A-B, main plots; see the dashed magenta curves). In addition, we

also used a moving average window procedure (see Methods), which markedly reduces the variance (Fig. 5, insets; see dark grey shaded curves superimposed on the original PSD in light grey).

The theoretical expressions for the transfer function were fit to the transfer functions reconstructed from the experiments. These fits were performed for a Warburg-type medium (Fig. 5, solid lines), for a resistive medium (dashed lines) and for purely capacitive medium (dashed red lines). Constrained to the frequency range of 3 Hz to 500 Hz, the fit was always markedly better for Warburg type impedances, for both cells shown in Fig. 5 and for both methods, as shown by the values of the residuals (see Table 1). Note that for a resistive-type medium, as well as for a purely capacitive medium, the parameter estimation (in particular for τ_m) always reached the boundaries of the constrained values, which is indicative that the obtained minimum in parameter space was far from optimal (even if the time constants may coincidentally reach realistic values). To confirm this, we allowed an unconstrained parameter fit and we observed that although the resistive-type would seemingly improve the fit (i.e., the initial plateau of the resistive-type curve would shift towards the 10-500 Hz range), it would however provide unrealistic parameter ranges. For the purely capacitive case, it was always impossible to achieve a good fit (i.e., slope zero). This is to be expected as the numerator of Eq. 29 grows quadratically and faster than the denominator, hence it behaves like the identity function, $y = f$, as frequency tends to infinity. Also note that the polynomial averaging algorithm of Appendix B always gave better results (see values of the residuals in Table 1), although performed on a dataset of higher variance (compare the grey lines in the main plots and insets of Fig. 5).

Note that the large difference in the residuals between the polynomial and moving average fits, in particular for the wargburg impedance, can be explained by the fact that the moving average does not fully eliminate the variance of the signal, while all the variance is virtually removed by the polynomial method (see magenta curves in Fig. 5A-B). The error increases even further for larger frequencies as the slope starts to change, possibly due to other phenomena, which the model does not capture. Also note that polynomial and moving average methods were compared in a previous study (see chapter 14 and Fig. 14.8.1 in [Press et al. (2008)]), which should be consulted for details. We stress that for the Warburg type medium that values obtained for τ_m and α are consistent with the data and theoretical predictions. In particular, the theory with Warburg impedance predicts that the values of α should be negligible for frequencies greater than

$1Hz$ (see Eqs. 53-54 in Appendix of ref. [Bédard and Destexhe (2009)]).

Similar results were also obtained for two other cells of the same database (not shown). The same results were also found by performing a similar analysis on another data set consisting of simultaneous intracellular and LFP recordings in awake cats (not shown; data from [Steriade et al. (2001a)], courtesy of Igor Timofeev, Laval University, Canada).
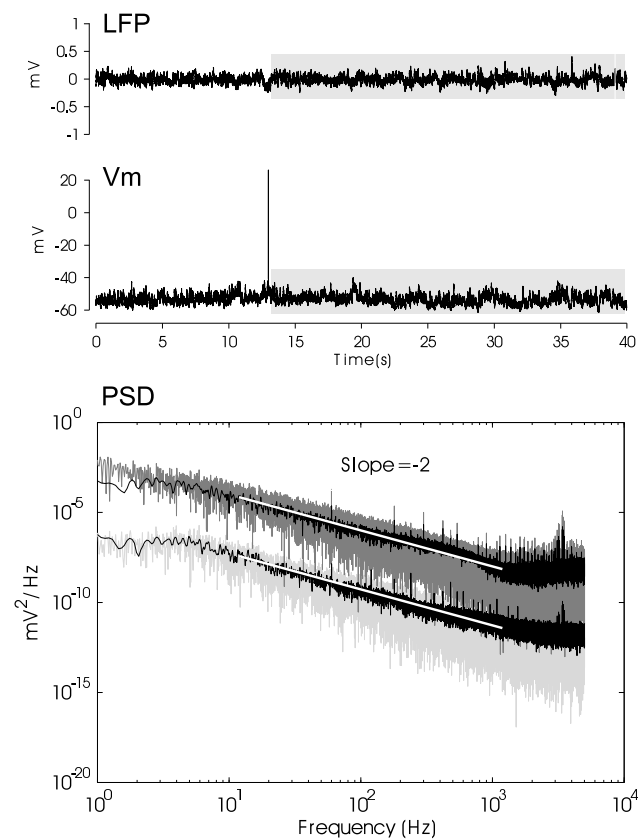
Fig. 4 Power spectra of simultaneous intracellular and LFP recordings in desynchronized states *in vivo*. The top panels depict the time series of simultaneously recorded bipolar LFP and V_m from rat barrel cortex in light anesthesia with low-amplitude desynchronized EEG (all recordings at zero current). The shaded grey box indicate the time period ($T \approx 38.69$ s) of subthreshold activity selected for analysis. The bottom panels are the calculated Power spectra (PSD) of both V_m (top plot in dark grey) and LFP (bottom plot in light grey), which show similar scaling. Superimposed, in black, are the moving average PSD with a window of $\sim 7.7sec$ (see Methods). This procedure results in a PSD with reduced variance but also reduced frequency resolution. The total number of points analyzed was N=386900 (between 2^{18} and 2^{19}). The similar scaling between V_m and LFP is highlighted by the overlaid white lines that have exactly *slope* $= -2$. In particular, the V_m scales with an exponent comprised between -2 and -2.4, while the LFP exponents range between -1.9 and -2.6.
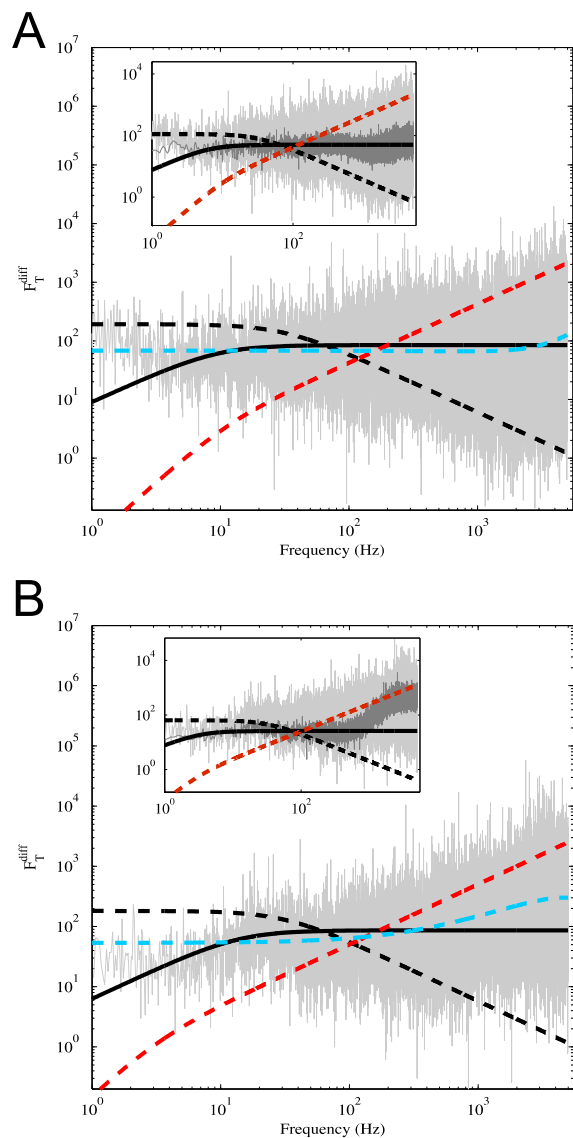
Fig. 5 Transfer function $F_T^{(diff)}$ computed from experimental data. The top panel corresponds to the cell shown in Fig. 4 and the bottom panel to a different cell. The experimentally calculated $F_T^{(diff)}$ (shown in light grey) shows an average slope of zero for frequencies between about 3 Hz and 500 Hz, and is compared to the best fits using a Warburg-type medium (solid black line), a resistive medium (black dashed line) and purely capacitive medium (red dashed line). Two different methods were used to calculate the best nonlinear least square fit, a polynomial averaging algorithm (main plots, third-order polynomial average shown as dashed blue curves; see Appendix B for details) and a moving average method which reduces the variance of the PSD (insets; see Methods). In both cases, the fit was constrained to frequencies between 3 and 500 Hz. The parameters of the respective fits are given in Table 1.

6 Discussion

In this paper, we have examined the transfer function between intracellular and extracellular potentials. By using a mean-field approximation in Fourier frequency

Cell	Impedance type	ε	τ_m	α
Cell 1	Warburg	3.4×10^2	17.5 ms	1.43
	Resistive	5×10^3	5 ms	194.94
	Capacitive	1×10^8	15 ms	0.001
Cell 1*	Warburg	3.2×10^5	14.8 ms	1.22
	Resistive	1.3×10^6	5 ms	111.74
	Capacitive	4.3×10^7	15 ms	0.010
Cell 2	Warburg	3.4×10^2	24.5 ms	1.3
	Resistive	5×10^3	5 ms	186.10
	Capacitive	7.8×10^7	50 ms	0.004
Cell 2*	Warburg	1.4×10^6	24.4 ms	1.28
	Resistive	1.7×10^6	5 ms	63.84
	Capacitive	9.3×10^6	50 ms	0.002

Table 1 Parameters for the fitting of the transfer function to experimental data for different types of extracellular impedance. $\varepsilon = ||y - \hat{y}(\tau_m, \alpha)||_2$: squared 2-norm of the fit residual, where y denotes the data and $\hat{y}(\tau_m, \alpha)$ represents the various models (Warburg, Resistive and Capacitive). τ_m: membrane time constant and $\alpha = \frac{R_m R}{kd}$ (refer back to equations in the main text), which are obtained by the fitting procedure. Cell 1 and Cell 2 correspond to a) and b) in Fig. 5; Cell 1* and 2* refer to the values obtained in the same cells using the moving average method (Fig. 5, insets).

space, we derived a method allowing us to obtain an expression relating the LFP with the intracellular V_m activity. The main theoretical finding is that this transfer function (which does not depend on the frequency spectrum of current sources) takes very different forms according to the type of frequency dependence of the extracellular medium, and thus could be used as a means to estimate which type of frequency dependence (if any) is most consistent with experiments. Second, we have applied this formalism to intracellular recordings in desynchronized EEG states, for which the mean-field approximation should best apply. We found that, in rat barrel cortex, the extracellular medium seems frequency dependent with a Warburg type impedance.

One key assumption of the present formalism is that individual synaptic currents sources are uncorrelated. There is ample evidence that this is the case for EEG-desynchronized states, as shown by the low levels of correlation between simultaneously recorded units [Contreras and Steriade (1996), Destexhe et al. (1999), Gawne and Richmond (1993), Steriade et al. (2001b), Zohary et al. (1994)], or by the low correlations between multi-site LFPs [Destexhe et al. (1999)]. However, there are limits to this assumption. First, dual recordings in awake mice barrel cortex showed that the subthreshold activities of neurons can display periods of significant correlation, even with desynchronized EEG [Poulet and Petersen (2008)]. Indeed, a certain level

of correlation is unavoidable from the redundant connectivity of neurons in cortex, although the activity itself can produce negative correlations which may cancel the effect of redundant connectivity [Renart et al. (2010)]. Second, it is evident that the activity cannot be totally decorrelated, otherwise the EEG amplitude would be close to zero [Gold et al. (2006)]. Nevertheless, the amplitude of the EEG during desynchronized states is considerably lower than during synchronized activity (such as slow waves), which is associated to a general decorrelation of neurons [Contreras and Steriade (1996)], and the present formalism should be applicable to such desynchronized states. Further studies should consider these points to build more realistic mean-field models of desynchronized states, which would lead to more realistic transfer functions.

In a previous investigation [Bédard and Destexhe (2009)], we have shown theoretically that several physical phenomena can lead to frequency dependence of the extracellular medium: ionic diffusion and membrane polarization. The former predicts an impedance of Warburg type ($Z \sim 1/\sqrt{f}$), while the latter predicts a capacitive-type impedance ($Z \sim 1/f$) [Bédard et al. (2006b)]. These two phenomena can also explain different experimental observations: the frequency dependent conductivity observed experimentally in brain tissue [Gabriel et al. (1996)] can be reproduced by a combination of these two mechanisms. Recent measurements from monkey cortex suggesting resistive medium [Logothetis et al. (2007)] can be explained by the fact that the influence of diffusion was avoided in that case. This technique is based on the saturation effect (Geddes effect, which is represented by Zener diodes in [Logothetis et al. (2007)]), which greatly diminishes the concentration gradient around the electrode, such that the ionic diffusion is more limited. A Warburg type impedance was also found to account for the $1/f$ power spectral structure of LFPs (see details in [Bédard and Destexhe (2009)]).

The present results are consistent with this analysis. The transfer functions measured here for 4 cells are all consistent with the Warburg type impedance of ionic diffusion up to 500 Hz. The other type of extracellular impedances mentioned above, either purely resistive or purely capacitive, could not fit the data (see Fig. 5). While these results seem to rule-out purely resistive or capacitive media, there is still a possibility that they apply outside the 3-500 Hz frequency range. For example, polarization phenomena, which can be modeled as a capacitive effect with a low cutoff frequency [Bédard et al. (2006b)], may contribute to the low frequency range (below 10 Hz). Further theoretical and

experimental work is needed to investigate these aspects. In particular, experiments should be carried with controlled current sources as close as possible to the biological current sources, for example using micropipettes.

It is important to keep in mind that the present method derives from a mean-field approach in frequency space, and thus relies on the assumption that individual current sources are independent. This justifies the use of desynchronized EEG states, in which synaptic current sources are expected to have very low correlation. The simulations presented in Fig. 2 (bottom panels) show that the LFP predicted by a compartmental dendritic model is virtually identical to that obtained by individual compartments, which suggests that considering a set of independent sources is not a bad approximation. However, if strong correlations occur, such as during synchronized population activities, the current sources may no longer be considered as independent, and another formalism should be used.

A recent study on modeling extracellular action potentials [Pettersen and Einevoll (2008)] showed that the cable structure of neurons can also cause low-pass filtering, because the return current is itself filtered by the membrane capacitance. This is a clear example where the correlation between current sources cannot be neglected. However, we showed here that such a contribution is negligible for *in vivo* conditions (Fig. 2A,B), presumably because the axial currents are very small compared to the intense synaptic currents. So far, the only plausible physical cause to explain the observed $1/f$ filtering under *in vivo* conditions is ionic diffusion (for frequencies up to 500 Hz). It is possible that for states of reduced synaptic activity, the filtering due to morphology plays a role, although this still needs to be demonstrated experimentally Further studies should investigate these aspects by constraining these different theories by appropriate experiments.

One major criticism to the previous measurement techniques [Ranck (1963), Gabriel et al. (1996), Logothetis et al. (2007)] is that they use current intensities of one or several order of magnitude larger than biological sources, and these currents evidently interact with the medium very differently as natural sources. The present method has the advantage of not suffering from this limitation, because it is using only passive recordings of physiological signals, with no need of injecting currents. This method should therefore be considered as complementary to direct measurements.

Finally, the expression given by Eqs. 24 and 26 could be used to directly estimate the impedance of the extracellular medium as a function of frequency (still within the mean-field approximation). We did not attempt this type of approach here, but instead considered different hypotheses concerning the impedance of the medium. The present analysis reported here for 4 cells was also confirmed by using two cells from another database of intracellular recordings in desynchronized EEG states in awake animals (courtesy of I. Timofeev, Laval University, Canada), which also indicated a Warburg type impedance (not shown). The same approach should be extended to a much larger sample of cells and brain states, to provide a full estimate of the impedance spectrum of the medium. The present results therefore must be considered as preliminary and must be confirmed by using further analyses of simultaneously recorded LFPs and intracellular recordings during desynchronized EEG states *in vivo*.

Appendix A: impedance for non-ideal membranes

In this section, we derive the expressions for the impedance of non-ideal membranes, which take into account that the membrane capacitance cannot be charged instantaneously (see Bedard and Destexhe, 2008). Still within the linear regime and for a spherical source, we have:

$$
\begin{aligned}
I_r &= \sum_{i=1}^{N} g_i\,(t, V_m)(V_m(t) - E_i) \\
I_c &= C_m \frac{dV_c}{dt} \\
I_m &= I_r + I_c \\
V_m &= V_c + R_{\mathrm{MW}} C_m \frac{dV_c}{dt} = V_c + \tau_{\mathrm{MW}} \frac{dV_c}{dt}
\end{aligned}
\tag{30}
$$

where all parameters have the same definition as in the main text, except for r_{MW}, which is the Maxwell-Wagner resistance which gives the non-ideal aspect of the membrane capacitance. The associated time constant, τ_{MW}, is also known as "Maxwell-Wagner time".

In the linear regime, we have

$$\Delta I_r = \sum_{i=1}^{N} g_i \left(\langle V_m \rangle |_t \right) \Delta V_m$$

$$\Delta I_c = C_m \frac{d\Delta V_c}{dt}$$

$$\Delta I_m = \Delta I_r + \Delta I_c \tag{31}$$

$$\Delta V_m = \Delta V_c + \tau_{\text{MW}} \frac{d\Delta V_c}{dt}$$

Thus, in these conditions, the system of equations associated to the membrane is linear with time-independent coefficients.

By expressing the variation of current produced by the cell as a function of the variation of membrane voltage, in Fourier space, we obtain:

$$\Delta I_r(f) = G_m \Delta V_m(f)$$

$$\Delta I_c(f) = i\omega C_m \Delta V_c(f)$$

$$\Delta I_m(f) = \Delta I_r(f) + \Delta I_c(f) \tag{32}$$

$$\Delta V_m(f) = \Delta V_c(f) + i\omega \tau_{\text{MW}} \Delta V_c(f)$$

where

$$G_m = \sum_{i=1}^{N} g_i$$

.

It follows that the membrane impedance is given by:

$$Z_m(f) = \frac{\Delta V_m(f)}{\Delta I(f)} = \frac{R_m}{1 + i\frac{\omega \tau_m}{1 + i\omega \tau_{\text{MW}}}} \tag{33}$$

where $R_m = \frac{1}{G_m}$. Note that if we set $\tau_{\text{MW}} = 0$, we recover the same expressions for the impedance of ideal membranes, as considered in the main text.

Appendix B: Polynomial averaging algorithm for frequency-dependent signals

The polynomial averaging technique consists of fitting a polynomial to the cumulative distribution of the amplitude of the signal in frequency space. According to this procedure, one evaluates the difference between the data and model via a minimization problem (in the frequency space) as follows

$$argmin_{\tau_m, \alpha} ||y(f) - \hat{y}(f, \tau_m, \alpha)||, \quad f \in [3Hz, 500Hz], \tag{34}$$

where $y(f)$ represents the transfer function (after a Fourier transform or PSD has been applied). $\hat{y}(\cdot)$ represent the various model transfer functions (i.e. Warburg, resistive or capacitive) parameterized by τ_m and α. Since the theory we develop only explains changes in the slope of the mean of $y(f)$, then to a first order approximation the above equation can be re-written in the following way

$$argmin_{\tau_m, \alpha} ||<y>(f) - \hat{y}(f, \tau_m, \alpha)||, \quad f \in [3Hz, 500Hz] \tag{35}$$

where the operator $< \cdot >$ is the mean of the data in frequency domain. Any technique can be taken to evaluate the mean such as the moving average. However, the moving average does not completely remove the variance and is not general enough. Since Fourier transform of the transfer function or its PSD show a large variance we remove entirely this variance by employing the following polynomial algorithmic filter.

1. The Fourier transform of the signals is integrated relative to frequency:

$$G(f) = \int_{f_{min}}^{f} F(f') df' \tag{36}$$

where f_{min} is the minimal frequency considered with $f \leq F_{max}$, and $F(f')$ is the signal for which the mean function must be obtained. This integration gives a function of frequency which is very close to the integral of the mean function, which is true for the signals considered here.

2. To smooth the function $G(f)$, a minimum variance fit is performed using a third-degree polynomial:

$$G^*(f) = A_3 f^3 + A_2 f^2 + A_1 f + A_0 + O(f^4). \tag{37}$$

Note that higher-order polynomials can be used to improve accuracy. However, in our case we did not observe any gain for orders larger than three.

3. This polynomial was formally derived to find the expression of the mean function $<F>(f)$

$$<F>(f) = \frac{dG^*}{df} = 3A_3 f^2 + 2A_2 f + A_1. \tag{38}$$

Note that this algorithm is general and does not depend on any hypothesis concerning the stationarity of the

signal because the average function is calculated in Fourier space.

Acknowledgments

References

Bédard et al. (2004). Bédard, C., Kröger, H., Destexhe, A. (2004). Modeling extracellular field potentials and the frequency-filtering properties of extracellular space. *Biophys. J.* **64**:1829-1842.

Bédard et al. (2006a). Bédard, C., Kröger, H., Destexhe, A. (2006a). Does the 1/f frequency-scaling of brain signals reflect self-organized critical states ? *Phys. Rev. Lett.* **97**:118102.

Bédard et al. (2006b). Bédard, C., Kröger, H., Destexhe, A. (2006b). Model of low-pass filtering of local field potentials in brain tissue. *Phys. Rev. E* **73**:051911.

Bédard and Destexhe (2008). Bédard, C., Destexhe, A. (2008). A modified cable formalism for modeling neuronal membranes at high frequencies. *Biophys. J.* **94(4)**:1133-1143.

Bédard and Destexhe (2009). Bédard, C., Destexhe, A. (2009). Macroscopic models of local field potentials and the apparent 1/f noise in brain activity. *Biophys. J.* **96(7)**:2589-4608.

Chari and Salon (1999). Chari M.V.K. and S.J. Salon (1999). *Numerical Methods in Electromagnetism*, Academic Press, New York.

Contreras and Steriade (1996). Contreras D and Steriade M. (1996) State-dependent fluctuations of low-frequency rhythms in corticothalamic networks. *Neuroscience* **76**: 25-38.

Destexhe et al. (1999). Destexhe, A., Contreras D., Steriade, M. (1999). Spatiotemporal analysis of local field potentials and unit discharges in cat cerebral cortex during natural wake and sleep states. *J. Neurosci.* **19**:4595-4608.

Destexhe et al. (2001. Destexhe, A., Rudolph, M., Fellous, J-M. and Sejnowski, T.J. (2001) Fluctuating synaptic conductances recreate in-vivo–like activity in neocortical neurons. *Neuroscience* **107**: 13-24.

Destexhe et al. (2003. Destexhe, A., Rudolph, M. and Paré, D. (2003) The high-conductance state of neocortical neurons *in vivo*. *Nature Reviews Neurosci.* **4**: 739-751.

El Boustani et al (2009). EL Boustani, S., Marre, O., Béhuret, S., Baudot, P., Yger, P., Bal, T., Destexhe, A. and Frégnac, Y. (2009) Network-state modulation of power-law frequency-scaling in visual cortical neurons. *PLoS Computational Biol.* **5**: 1-18.

Erchova and McGonigle (2008). Erchova, I., McGonigle, D. J. (2008). Rhythms of the brain: An examination of mixed mode oscillation approaches to the analysis of neurophysiological data *Chaos* **18**:015115.

Gabriel et al. (1996). Gabriel, S., Lau, R.W., Gabriel, C. (1996). The dielectric properties of biological tissues : II. Measurements in the frequency range 10 Hz to 20 GHz. *Phys. Med. Biol.* **41**:2251-2269.

Gawne and Richmond (1993). Gawne TJ and Richmond BJ. (1993) How independent are the messages carried by adjacent inferior temporal cortical neurons? *J. Neurosci.* **13**: 2758-2771.

Gold et al. (2006). Gold, C., D.A. Henze, C. Koch, and G. Buzsaki. (2006) On the origin of the extracellular action potential waveform: A modeling study. *J. Neurophysiol.* **95**: 3113-3128.

Hines and Carnevale (1997). Hines M and Carnevale N (1997) The neuron simulation environment. *Neural Computation* **9**: 1179–1209.

Jefferys (1995). Jefferys, J. G. R. (1995). Nonsynaptic modulation of neuronal activity in the brain: Electric currents and extracellular ions. *Physiological Reviews* **75 (4)**:689-714.

Katzner et al. (2009). Katzner S., Nauhaus I., Benucci A., Bonin V., Ringach D. L., Carandini M. (2009). Local origin of field potentials in visual cortex. *Neuron* **61**:35-41.

Logothetis et al. (2007). Logothetis, N. K., Kayser, C., Oeltermann, A. (2007). In vivo measurement of cortical impedance spectrum in monkeys: Implications for signal propagation. *Neuron* **55**:809-823.

Nunez and Srinivasan (2006). Nunez, P. L., Srinivasan, R. (2006) Electric Fields of the Brain: The neurophysics of EEG. *Oxford University Press, New York*.

Pettersen and Einevoll (2008). Pettersen, K.H., Einevoll, G. (2008). Amplitude Variability and Extracellular Low-Pass Filtering of Neuronal Spikes *Biophys. J.* **94(3)**:784-802.

Poulet and Petersen (2008). Poulet JF and Petersen CC. (2008) Internal brain state regulates membrane potential synchrony in barrel cortex of behaving mice. *Nature* **454**: 881-885.

Press et al. (2008). Press, W., Teukolsky P., Vetterlin W., Flannery B. (2008). Numerical Recipes in C: The art of scientific computating. *ISBN 0-521-43108-5*

Ranck (1963). Ranck, J.B., Jr. (1963) Specific impedance of rabbit cerebral cortex. *Exp. Neurol.* **7**:144-152.

Renart et al. (2010). Renart A, de la Rocha J, Bartho P, Hollender L, Parga N, Reyes A and Harris KD. (2010) The asynchronous state in cortical circuits. *Science* **327**: 587-590.

Rudolph et al. (2005). Rudolph, M., Pelletier J.G., Paré, D. and Destexhe, A. (2005) Characterization of synaptic conductances and integrative properties during electrically induced EEG-activated states in neocortical neurons in vivo. *J. Neurophysiol.* **94**: 2805-2821.

Steriade et al. (2001a). Steriade M, Timofeev I, Grenier F. (2001a). Natural waking and sleep states: a view from inside neocortical neurons. *J. Neurophysiol.* **85**:1969-1985.

Steriade et al. (2001b). Steriade M. (2001b). *The Intact and Sliced Brain*. MIT Press, Cambridge, MA.

Yaron-Jakoubovitch et al (2008). Yaron-Jakoubovitch, A., Jacobson, G.A., Koch, C., Segev, I. and Yarom, Y. (2008) *A paradoxical isopotentiality : a spatially uniform noise spectrum in neocortical pyramidal cells.*. *Frontiers in Cellular Neuroscience* **2**: 1-9.

Wilent and Contreras (2005a). Wilent, W.B. and Contreras, D. (2005a). Dynamics of excitation and inhibition underlying stimulus selectivity in rat somatosensory cortex. *Nature Neurosci.* **8**:1364-1370.

Wilent and Contreras (2005b). Wilent, W.B. and Contreras, D. (2005b). Stimulus-dependent changes in spike threshold enhance feature selectivity in rat barrel cortex neurons. *J. Neurosci.* **25**:2983-2991.

Zohary et al. (1994). Zohary, E., Shadlen, M.N., and Newsome, W.T. (1994). Correlated neuronal discharge rate and its implications for psychophysical performance. *Nature* **370**:140-143.